Nanocrystalline TiO₂(B) as Anode Material for Sodium-Ion Batteries

Liming Wu,[a,b,c] Dominic Bresser,[a,b,c,*] Daniel Buchholz,[a,b,c] and Stefano Passerini[a,b,c,**,z]

[a]*Institute of Physical Chemistry & MEET Battery Research Centre, University of Muenster, 48149 Muenster, Germany*
[b]*Helmholtz-Institute Ulm, Electrochemistry I, 89081 Ulm, Germany*
[c]*Karlsruher Institute of Technology, 76344 Eggenstein-Leopoldshafen, Germany*

High surface area, nanostructured, and phase-pure TiO₂(B) noodles-like secondary particles were successfully synthesized by a facile one-pot synthesis, based on the hydrolysis of TiCl₃ using a mixture of ethylene glycol and water at moderate temperature. The primary nanoparticles have a uniform size and are about 15 nm in diameter as determined by TEM analysis and exhibit an increased exposure of the (010) facet as indicated by XRD analysis. Unlike the electrochemical reaction with lithium, the application as sodium-ion electrode material reveals substantial differences, including the initial amorphization of the TiO₂(B) particles, accompanied by a partial irreversibility of the sodium storage, presumably related to sodium trapping inside the active material particles and the absence of a stable solid electrolyte interphase, as indicated by galvanostatic cycling and electrochemical impedance spectroscopy, respectively. Besides, TiO₂(B)-based electrodes show a stabilized reversible capacity of about 100 mAh g⁻¹ and a very good C rate capability.

While sodium-ion batteries were initially considered only as low-cost alternative for lithium-ion batteries with a particular focus on their application as stationary energy storage devices,[1–3] recent developments indicated that such devices might provide even similar energy densities in case suitable cathode and anode active materials are combined.[4–6] However, particularly regarding the anode side, the identification of long-term stable, environmentally friendly, and abundant active materials, providing high specific capacities and operating at a reasonably low potential, is still considered to be one of the major challenges for this technology.[4,6,7] So far, research activities basically focused on hard carbons,[8–14] organic compounds like sodium terephthalate or carboxylates,[15–18] alloying materials such as Sn,[19–27] Sb,[28,29] or Ge,[30] conversion materials,[31–34] or titanium-based insertion materials like Na₂Ti₃O₇[35–37] or Li₄Ti₅O₁₂.[38] Generally, insertion materials offer substantial advantages compared to alloying or conversion materials with respect to safety issues, long-term cycling stability, and frequently also environmental friendliness as well as natural abundance. Following the trend of investigating active materials, which are already known to be suitable candidates for lithium-ion batteries, recently also various TiO₂ polymorphs have attracted great interest like anatase TiO₂,[39–45] amorphous TiO₂,[46] or TiO₂(B).[47] Among these, the best results in terms of specific capacity, long-term cycling stability, and high rate capability were certainly reported for anatase TiO₂.[40–43] However, the reversible sodium storage mechanism is obviously different from the classic (de-)insertion mechanism known for lithium,[48–53] as an initial reduction of TiO₂ to metallic titanium and an amorphous sodium titanate occurs.[42] TiO₂(B) is a very well performing anode material for lithium-ion applications,[54–60] but so far – to the best of our knowledge – only one study reported its application as sodium-ion active material. The electrochemical performance, which might be best described by a rather rapid initial capacity fading and a low reversible capacity of about 50 mAh g⁻¹, is certainly not that promising,[47] although this might be also related to the cut-off potentials of 3.0 and 0.8 V vs. Na/Na⁺. Besides, the authors observed a rather huge expansion of the (001) plane interlayer spacing (from

0.56 nm to about 0.64–0.68 nm) accompanied by the co-existence of Ti³⁺ and Ti⁴⁺ at the nanotubes surface, while the general morphology of the tubes remained after sodiation. Consequently, a solid solution mechanism for the reversible sodium ion (de-)insertion comparable to the lithium ion storage mechanism was proposed.

Herein, however, we show that TiO₂(B) – similarly to anatase TiO₂ – presents a rather different electrochemical behavior as sodium-ion electrode material compared to lithium-ion applications. In fact, the nanostructured TiO₂(B) noodle-like secondary particles, synthesized by a facile one-pot synthesis, become fully amorphous upon the initial sodiation. Upon continuous (de-)sodiation the capacity initially decreases, presumably related to irreversible sodium trapping inside the host structure and the absence of a stable solid electrolyte interphase (SEI), before it finally stabilizes at about 102 mAh g⁻¹, i.e., more than twice the capacity reported in the previous study by Huang et al.[47]

Experimental

Synthesis.— Nanocrystalline TiO₂(B) was synthesized following a recently reported method by Xiang et al.[61] Briefly, TiCl₃ (Sigma-Aldrich, 99.995%) was hydrolyzed under argon atmosphere using a mixture of ethylene glycol (Sigma-Aldrich, 99.8%) and deionized water.[61] In a typical synthesis, 0.3 g of TiCl₃ were dissolved in 38 mL ethylene glycol and 2 mL deionized water. This mixture was then transferred to a 50 mL Teflon-lined autoclave. The temperature was kept constant at 160°C for 6 h. After cooling down to room temperature, the obtained solid product was separated from the liquid phase by centrifugation and subsequently rinsed several times using ethanol and deionized water. Finally, the white solid product was dried under vacuum overnight prior to any further characterization.

Morphological and structural characterization.— The structure and morphology of the synthesized TiO₂(B) nanoparticles was characterized by means of X-ray diffraction (XRD, BRUKER D8 Advance; Cu-Kα radiation, λ = 0.154 nm), scanning electron microscopy (SEM, ZEISS Auriga), and transmission electron microscopy (TEM, ZEISS Libra 200FE, accelerating voltage: 200 kV). For the latter, the TiO₂(B) nanopowder was dispersed in C₂H₅OH and a few drops of this dispersion were placed on a carbon-coated copper grid. The Brunauer-Emmett-Teller (BET) surface area was determined by

*Electrochemical Society Student Member.
**Electrochemical Society Active Member.
zE-mail: stefano.passerini@kit.edu

nitrogen adsorption measurements using an ASAP 2020 (Accelerated Surface Area and Porosimetry Analyzer, MICROMERITICS).

Electrochemical characterization.— For the electrochemical characterization, $TiO_2(B)$ electrodes were prepared having a final composition of 70 wt% $TiO_2(B)$, 20 wt% conductive carbon (SuperC65, TIMCAL), and 10 wt% sodium carboxymethyl cellulose (CMC, WALOCEL CRT 2000 PPA 12, Dow Wolff Cellulosics). For comparison, also electrodes based on conductive carbon only were prepared having a final composition of 90 wt% conductive carbon and 10 wt% CMC, following the same electrode preparation procedure. Firstly, CMC was dissolved in deionized water to obtain a 2.5 wt% solution. Then the conductive carbon and $TiO_2(B)$ were added and the resulting mixture was dispersed by ball milling for 3 h. The obtained slurry was then cast on dendritic copper foil (SCHLENK). After drying at room temperature, disk electrodes (Ø = 12 mm) were punched and dried for 24 h at 120°C under vacuum. The active material mass loading of the thus obtained electrodes was about 1.5 mg cm^{-2}. Three-electrode Swagelok cells were assembled in an MBraun glove box with an oxygen and water content below 0.5 ppm. Sodium metal (99.8%, ACROS ORGANICS) was used as counter and reference electrode. Accordingly, all potential values given in this manuscript refer to the Na/Na$^+$ reference couple. A sheet of Whatman glass fiber was used as separator and drenched with a 1 M solution of $NaClO_4$ (98% SIGMA ALDRICH) in a 1:1 mixture of propylene carbonate (PC, SIGMA ALDRICH) and ethylene carbonate (EC, UBE), serving as electrolyte. As very recently reported, this electrolyte composition showed the best results in terms of electrochemical performance in combination with nanoparticulate anatase TiO_2-based electrodes.[40] Galvanostatic cycling and cyclic voltammetry were carried out utilizing a Maccor Battery Tester 4300 and VMP3 Potentiostat (BIOLOGIC), respectively. A C rate of 1 C corresponds to an applied specific current of 335 mA g^{-1}. All electrochemical studies were performed at ambient temperature (20 ± 2°C).

Electrochemical impedance spectroscopy (EIS) was carried out by means of a Solartron 1250 Frequency Response Analyzer with either an EG&G potentiostat/galvanostat model 273 or a Solartron 1286 electrochemical interface in a two-electrode configuration. The frequency ranged from 75 kHz to 10 mHz, recording six points per decade when the frequency decreased. All EIS studies were carried out in the charged (desodiated) state of the $TiO_2(B)$-based electrodes.

In situ XRD & ex situ SEM.— In situ XRD analysis of the electrochemical (de-)sodiation of $TiO_2(B)$ was performed with a self-designed in situ cell as described in detail already in previous studies.[42,62,63] For the electrode preparation, 0.01 g of CMC was dissolved in 0.8 mL of deionized H_2O. Subsequently, 0.07 g of $TiO_2(B)$ and 0.02 g of conductive carbon were added. The resulting mixture was dispersed by means of ball milling for 3 h and the obtained slurry was cast on a beryllium window (thickness = 200 µm, Brush Wellman), which served simultaneously as current collector and "window" for the X-ray beam. The coated Be window was dried at 80°C for 10 minutes and at 40°C under vacuum overnight. Metallic sodium foil served as counter and reference electrode. Two sheets of Whatman glass fiber, which served as separator, were drenched with 500 µL of 1 M $NaClO_4$ in EC:PC (1:1 by volume). The assembled cell rested overnight. Subsequently, the cell was galvanostatically cycled by means of a Solartron 1287 potentiostat, applying a specific current of 0.0133 A g^{-1}, calculated according to a complete discharge in about 30 h. In parallel, XRD analysis was performed, using a 2θ range of 12° to 65°, with a step size of 0.019° and a time per step of 0.5 sec, resulting in a complete scan every 30 minutes, including an initial rest period of 405 sec before every scan. After discharging to 0.1 V, the cell was charged to an upper cut-off potential of 2.0 V.

For the ex situ SEM characterization, the cycled cell was disassembled in an MBraun glove box (O_2 and H_2O <0.5 ppm). The electrode was then collected and rinsed using PC. Afterwards it was dried under vacuum at room temperature before it was transferred to the SEM

utilizing a self-designed sample holder in order to prevent any contact to air or moisture.

Results and Discussion

Morphological and structural characterization.— SEM analysis of the obtained white powder reveals the formation of secondary particles having a noodle-like morphology, more precisely the shape of a bunch of noodles, having an average particle size of about 250–350 nm (Figure 1a and 1b). These secondary particles, i.e., these bunches of noodles, however, are not formed out of monocrystalline noodle-like particles as maybe suggested initially. Instead, the single noodles appear to be polycrystalline and consist of very fine, almost spherical nanoparticles with a diameter of about 10–20 nm as observed by TEM analysis (Figure 1c and 1d). The small primary particle size leads to a very high porosity of the secondary particle structures, as evidenced by the extremely high BET surface area of about 216.9 m^2 g^{-1}. The obtained morphology is a little surprising as Xiang et al.[61] reported the preparation of 1.1 nm thick nanosheets using basically the same synthesis method. We assume that this different particle morphology might be related to a different composition of the ethylene glycol/H_2O mixture, the applied temperature, or the longer reaction time (6 h vs. 4 h[61]). Further studies will have to be performed to allow a more in-depth investigation of the dependency of these parameters and the resulting particle size, but this is beyond the scope of this manuscript. Generally, this synthesis method offers the great advantages of being rather simple and environmentally friendly, since the formation of $TiO_2(B)$ occurs in only one step and the utilized ethylene glycol might be recycled after the synthesis.[61] More important, the resulting material appears phase-pure (Figure 2) from XRD analysis and the obtained pattern matches very well the results reported by Xiang et al.[61] Moreover, it may be noticed that in accordance with this previous study[61] the (020) reflection is slightly higher in intensity compared to previous results indicating an increased surface exposure of the (010) facet. Considering that lithium ions are preferably inserted perpendicular to this facet[58] an increased exposure of this surface facet should result also in an enhanced sodium ion insertion, assuming a similar reaction mechanism.

Cyclic voltammetry.— Cyclic voltammetry (CV) is generally a very powerful and sensitive method to identify, investigate, and evaluate electrochemical reactions related to faradaic redox processes. Accordingly, in a first step we subjected $TiO_2(B)$-based electrodes to cyclic potentiodynamic sweeps setting the reversing potentials to 0.02 and 2.0 V vs. Na/Na$^+$ (Figure 3a). Apparently, the current response upon the initial cathodic sweep is constantly higher than for the subsequent cathodic scans starting from about 1.2 to 1.1 V indicating that there are some irreversible reactions occurring, presumably related to electrolyte decomposition. In fact, the starting potential for this electrolyte decomposition is in good agreement with a recent finding for anatase TiO_2-based electrodes.[40] The increasing specific current at the end of the scan, at about 0.02 V as well as the current peak at slightly higher potential upon the subsequent anodic scan is attributed to the reversible sodium storage in the comprised conductive carbon.[37,40] In order to decrease the contribution of the conductive carbon, we increased the lower reversing potential to 0.1 V (Figure 3b). Nonetheless, apart from a very little pronounced, rather broad cathodic and anodic peak at about 0.6 V and 0.9 V, respectively, presumably related to the reduction of Ti^{4+} to Ti^{3+} and the subsequent oxidation back to Ti^{4+}, no significant cathodic or anodic current peak feature is observed, neither for the initial sweep nor for the following ones, which is obviously different from nanoparticulate anatase TiO_2.[40,42] The co-existence of Ti^{3+} and Ti^{4+} was previously reported by Huang et al.[47] performing ex situ XPS on discharged $TiO_2(B)$ nanotubes (cathodic cut-off potential: 0.8 V). However, since XPS is a surface sensitive technique, the reduction of Ti^{4+} might be related to a superficial charge transfer, i.e., a pseudo-capacitive sodium storage, rather than sodium insertion into the bulk particle – at least at such rather
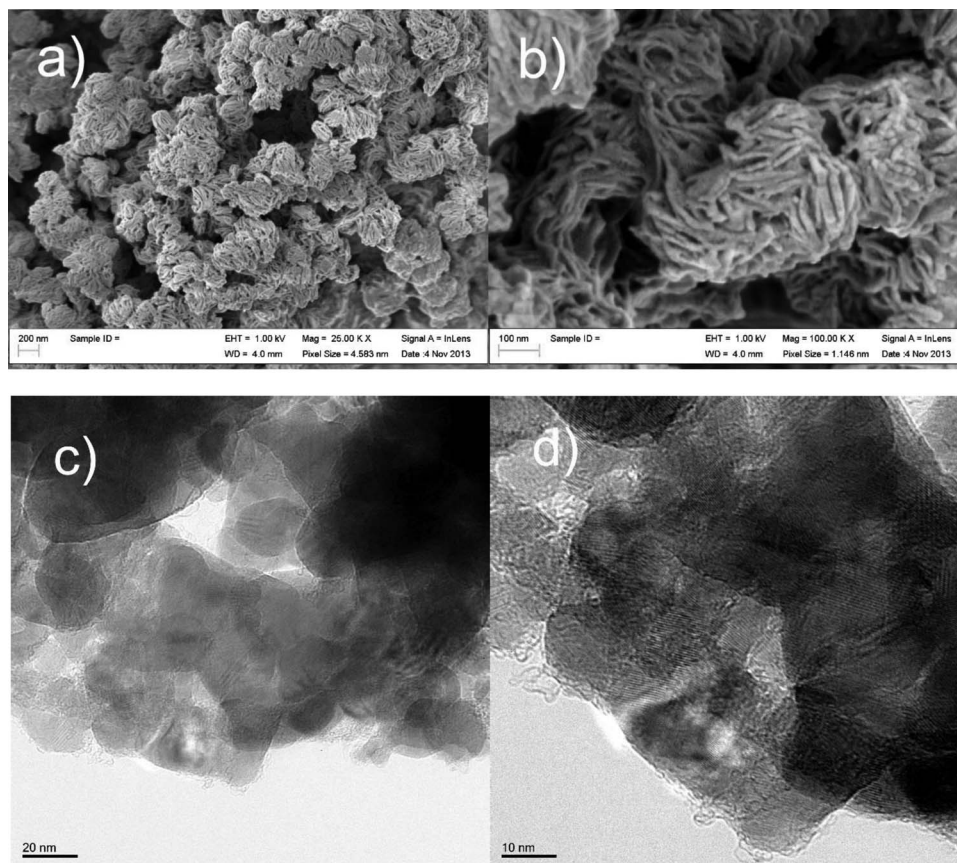
Figure 1. SEM images of the as-prepared nanocrystalline TiO$_2$(B) at a magnification of 25 kx (a) and 100 kx (b) as well as TEM images at a magnification of 250 kx (c) and 500 kx (d).

high potential. Generally, however, the CV response follows the trend of amorphous TiO$_2$.[64]

In situ XRD.— In a next step, XRD analysis coupled to galvanostatic discharge (sodiation) and charge (desodiation), i.e., in situ XRD analysis, was performed to gain some further insight into the reversible sodium storage mechanism in TiO$_2$(B). The corresponding potential profile of the first discharge and charge is presented in Figure 4a. While the potential decrease is initially rather sloped, a short plateau-like feature is observed at about 1.1 to 1.2 V. According to previous studies on anatase TiO$_2$ and the results obtained by performing cyclic
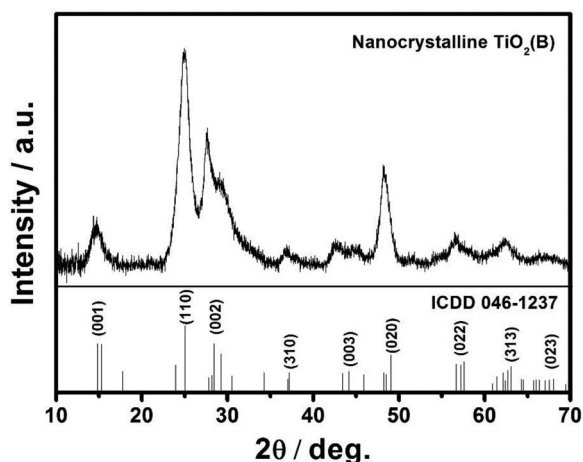

Figure 2. XRD pattern of the as-prepared TiO$_2$(B) material; the ICDD reference 046-1237 for TiO$_2$(B) is given in the bottom of panel (a).

voltammetry, this feature might be assigned to the cathodic decomposition of the electrolyte at the surface of the TiO$_2$(B) particles. This value is a little higher than for hard carbon-based electrodes,[6] which might be related to a catalytic effect of titanium oxide.[52] After this plateau-like feature, the potential decrease is again very sloped and no significant additional feature is observed. The series of XRD scans performed simultaneously with the galvanostatic discharge clearly reveals that the crystallinity of the active material decreases upon discharge (sodiation) and finally completely vanishes at the end of the discharge process (Figure 4b). Having a more detailed look at the most intense reflection (110) at about 25° (Figure 4c) reveals that up to scan #12, i.e., a potential of about 1.2 V, no substantial change of the pattern is observed. This observation confirms that the obtained capacity at such a potential basically originates from irreversible processes as electrolyte decomposition and SEI formation or (pseudo-)capacitive superficial sodium storage, which both do not affect the crystallinity of the active material. After scan #12 the (110) reflection starts to shift to lower 2θ values (indicated by the arrow in Figure 4d), revealing an increase of the lattice along this direction, presumably due to the insertion of sodium ions. At the same time the intensity decreases and the reflection is getting broader, so that finally at around 0.4 V (scan #29) no reflection can be detected anymore. Apparently, TiO$_2$(B) becomes fully amorphous, which might be a result of the initial sodium ion insertion causing sufficient strain on the crystallite structure to "randomly reorganize" induced by the substantially larger size of the sodium cations relatively to lithium.[65] It should be noted that the irreversible capacity in the first cycle is in general very high, suggesting that there might be other reasons than only electrolyte decomposition (despite the large surface area of the nanostructured, noodle-like TiO$_2$(B) particles) causing a loss of sodium, which is a further hint that the observed initial reorganization might also irreversibly trap sodium. In fact, very recently we were able to show that upon
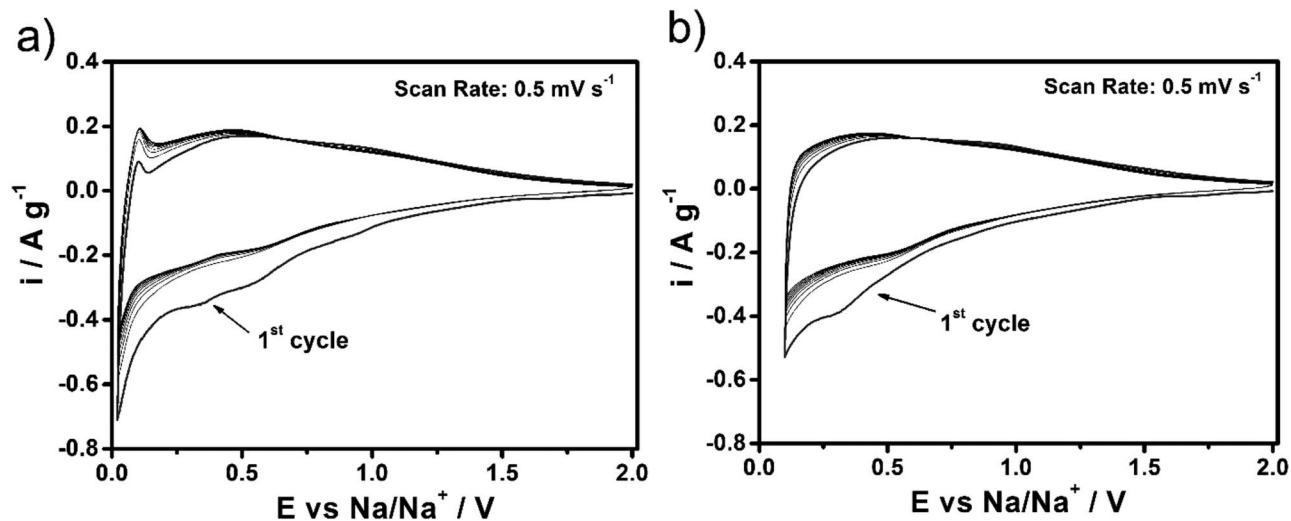
Figure 3. Cyclic voltammograms of TiO$_2$(B)-based electrodes, setting the reversing potentials to 0.02 V & 2.0 V (a) and 0.1 V & 2.0 V (b).
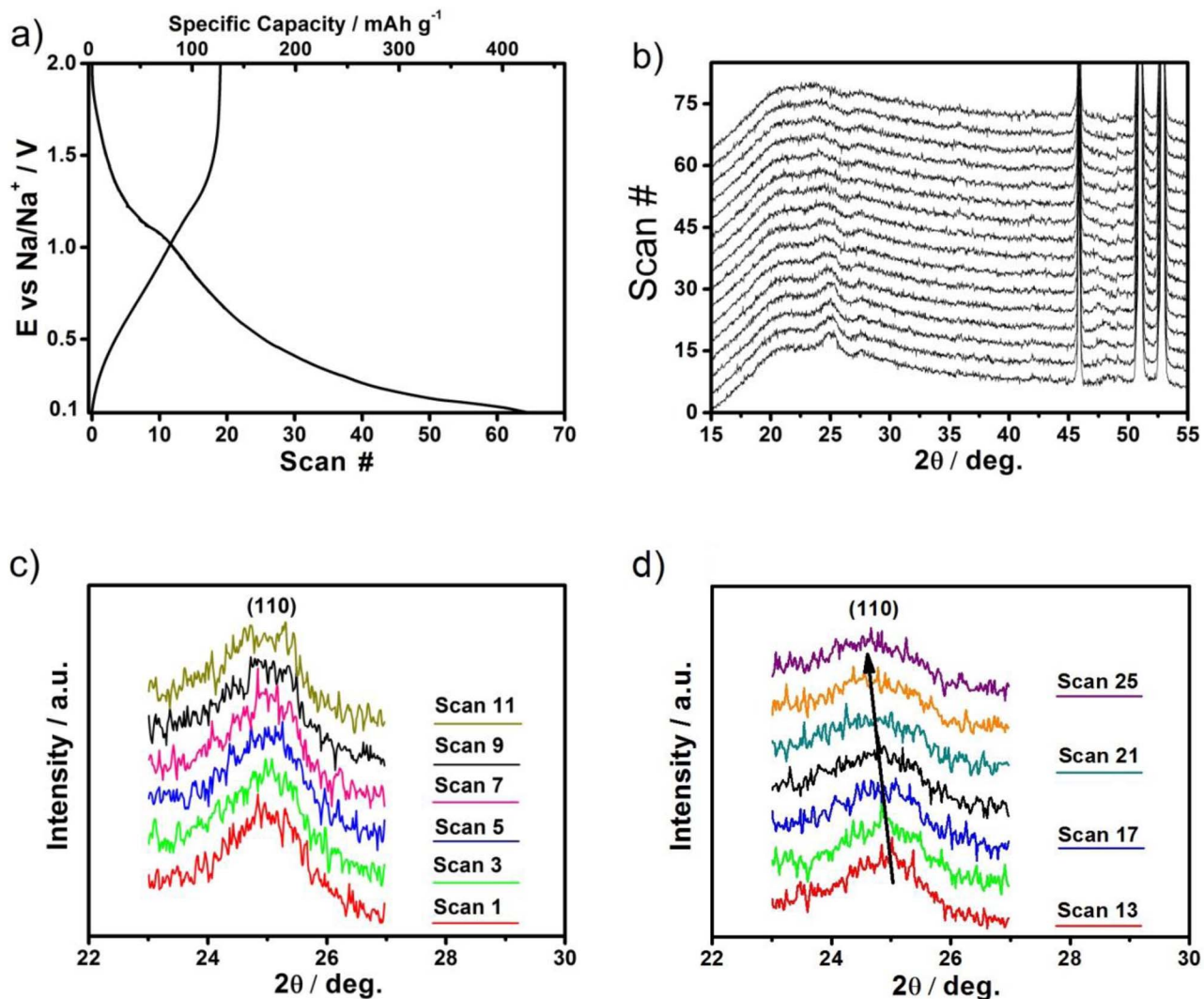

Figure 4. In situ XRD analysis of a TiO$_2$(B)-based electrode composite, galvanostatically discharged (sodiated) and charged (desodiated) applying a specific current of 13.3 mA g^{-1}; cut-off potentials: 0.1 and 2.0 V: a) the corresponding potential profile; b) the series of XRD patterns recorded upon discharge of the electrode composite, plotted in a waterfall-like diagram (for clarity reasons only every 4th scan is presented); c) and d) magnification of the (110) reflection showing the XRD patterns recorded upon selected scans.
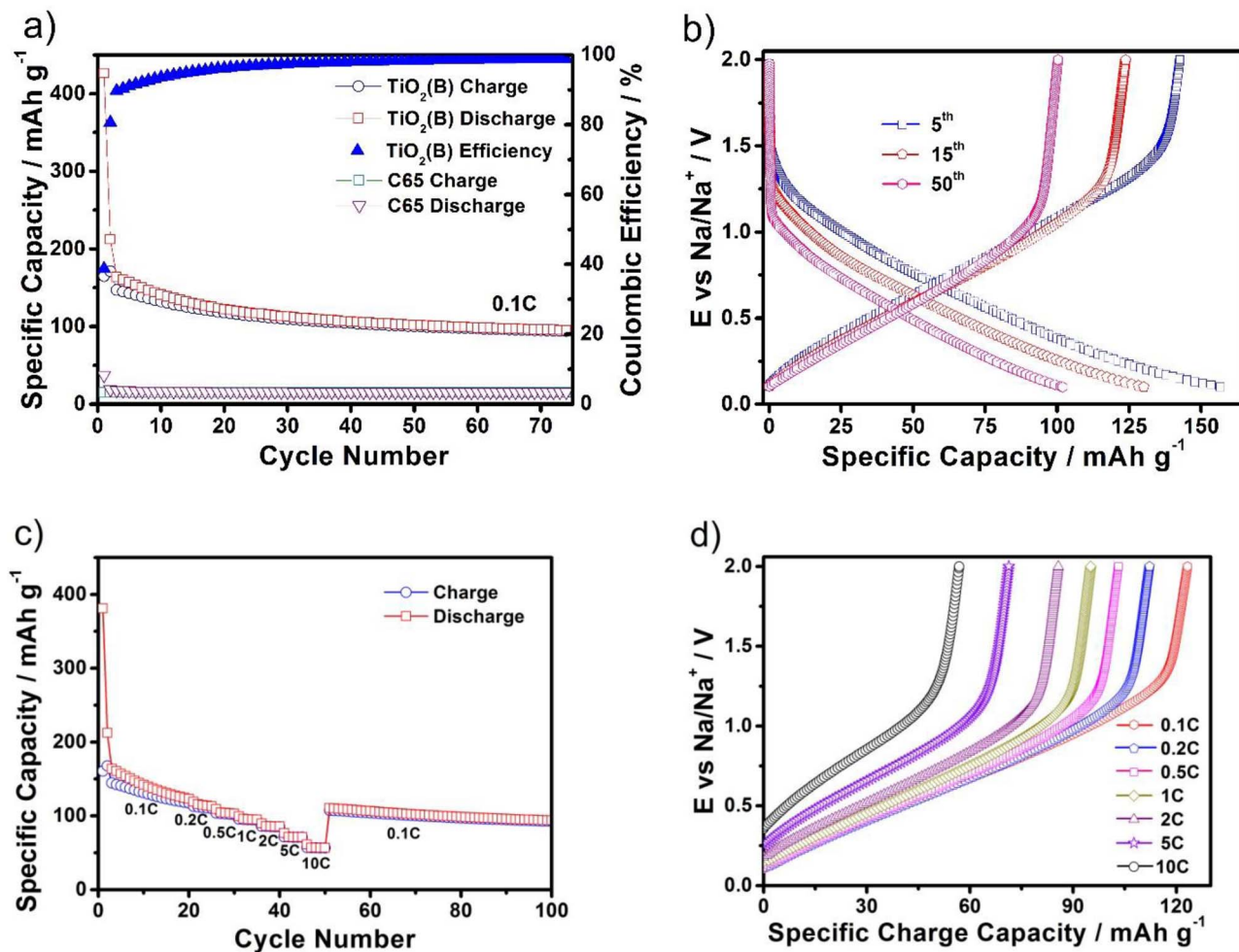
Figure 5. TiO$_2$(B)-based electrodes subjected to galvanostatic cycling: a) capacity vs. cycles at 0.1 C, cut-off potentials: 0.1 V and 2.0 V; two initial formation cycles at 0.01 C, cut-off potentials: 0.02 V to 2.0 V; the capacity contribution of the comprised conductive carbon (Super C65), derived from cycling a Super C65-based electrode (Figure S2), is also included; b) the corresponding potential profiles for selected cycles; c) capacity vs. cycles at various C rates: two formation cycles at 0.01 C (0.02 to 2.0 V) followed by constant current cycling at 0.1 C until the capacity has stabilized, subsequently the C rate was increased stepwise to 0.2, 0.5, 1, 2, 5, and 10 C (each 5 cycles) and finally set back to 0.1 C; d) corresponding potential profiles (charge process only) for selected cycles at each applied C rate.

sodiation of anatase TiO$_2$, sodium superoxide, metallic titanium, and amorphous sodium titanate are formed in the first discharge. Complementary studies will have to be performed in future to determine the detailed reasons for this large irreversibility also in case of TiO$_2$(B), which shows some similarities, but also several differences compared to anatase TiO$_2$.

Upon charge, then, the potential is steadily increasing up to about 1.3 V, before the increase is almost perpendicular to the x-axis and a further rise in potential is not accompanied by any specific capacity anymore (Figure 4a). The XRD patterns recorded during charge (Figure S1), however, do not show any change or any new reflections appearing and the structure remains amorphous.

Galvanostatic cycling.— Constant current cycling of TiO$_2$(B)-based electrodes shows quite interesting specific capacity values (Figure 5a). The origin of the initial huge irreversibility (1st discharge: 430 mAh g^{-1} & 1st charge: 185 mAh g^{-1} → coulombic efficiency: 40.9%) was already discussed. After two formation cycles, for which the lower cut-off potential was set to 0.02 V, the reversible capacity at 0.1 C is about 150 mAh g^{-1}, which is certainly a promising capacity for sodium-ion anode materials. The capacity contribution of the comprised conductive carbon is also shown in Figure 5a, confirming that the obtained capacity values basically refer to the TiO$_2$(B) active material. Nevertheless, while the coulombic efficiency increases upon

cycling up to 99.5% after 70 cycles, the reversible specific capacity decreases to 102 mAh g^{-1} at the 70th cycle. The reason for this fading is obviously related to a decreasing onset of the sodium ion insertion (Figure 5b). This decrease of the onset potential might originate from irreversibly trapped sodium inside the amorphous host structure, as the electrochemical potential of the active material for single phase insertion materials decreases with an increasing sodium content present already in the active material, i.e., the higher the sodium content, the lower the electrochemical potential, as reflected by the sloped potential profile (as a function of electrochemical potential of the active material in dependency on the overall sodium content).

Interestingly, comparing the potential profiles with those obtained for Nb$_2$O$_5$[66,67] (and, in fact also conductive carbon (Figure S2b)) reveals a rather similar shape, indicating that the sodium storage mechanism might, indeed, be similar. It has to be noted that it is not clear from the present results whether the active material is still TiO$_2$(B) (certainly not crystalline anymore within the XRD detection limits) or some (sodium) titanate or amorphous TiO$_2$, but due to the lack of a detailed knowledge on this issue, it is referred to the active material as TiO$_2$(B) throughout the whole manuscript.

The rate capability of TiO$_2$(B) is presented in Figure 4c and 4d. Indeed, the rate performance is very promising and the electrode provides specific capacities of around 150 mAh g^{-1}, 120 mAh g^{-1}, 100 mAh g^{-1}, 90 mAh g^{-1}, 80 mAh g^{-1}, 70 mAh g^{-1}, and 50 mAh
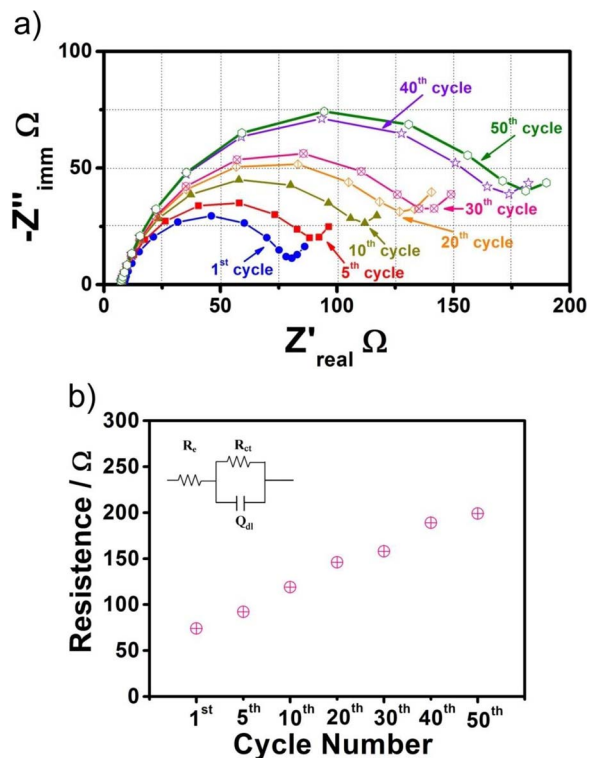
Figure 6. Electrochemical impedance spectroscopy (EIS) performed on TiO$_2$(B)-based electrodes in the fully charged (desodiated) state. Only experimental data obtained in the frequency range 75 kHz to 1.96 Hz are plotted for sake of clarity in the Nyquist plots (panel a). Panel (b) shows the development of the charge transfer resistance (at 6.32 Hz) upon cycling obtained fitting the experimental results into the model circuit presented as inset.

g^{-1} at 0.1 C, 0.2 C, 0.5 C, 1.0 C, 2.0 C, 5.0 C, and 10 C, respectively. Switching back to 0.1 C results in a specific capacity of about 125 mAh g^{-1}, which is in line with the previously described capacity fading (Figure 4a). Indeed, the capacity is still about 100 mAh g^{-1} after 100 cycles, being slightly better than the result obtained for constant current cycling at low rate (Figure 4a), indicating that the capacity fading might have another origin than a deterioration of the active material host structure, which would be even accelerated in case of applying elevated currents rather than being slowed down. The decrease in capacity for elevated C rates, however, is attributed simply to an increasing polarization (Figure 4d), which is commonly expected.

Electrochemical impedance spectroscopy & ex situ SEM.— For further investigation of the capacity decay upon cycling, EIS was carried out after a few selected cycles. For sake of clarity, Figure 6a illustrates the Nyquist plots in the frequency range (75 kHz to 1.96 Hz) relative to the electrode charge transfer process. Impedance data analysis was performed with the model circuit presented as inset in Figure 6b in which R$_e$ represents the electrolyte resistance (very stable upon cycling; see also Figure 6a), R$_{ct}$ is the charge transfer resistance, and Q$_{dl}$ is the associated double layer capacitance. Here, a constant phase element was used to take into account the slight depression of the charge transfer semi-circle commonly associated to the existence of an SEI layer.[68,69]

It is immediately obvious as the electrode charge transfer resistance increases upon cycling, starting from about 73 Ω in the first cycle to around 150 Ω in the 20th cycle and to about 195 Ω in the 40th cycle (Figure 6b). Such a continuous increase in resistance is related to an ongoing electrolyte decomposition on the TiO$_2$(B) nanoparticles surface, resulting in the continuous growth of the SEI layer. This was, indeed, confirmed by ex situ SEM characterization. The comparison
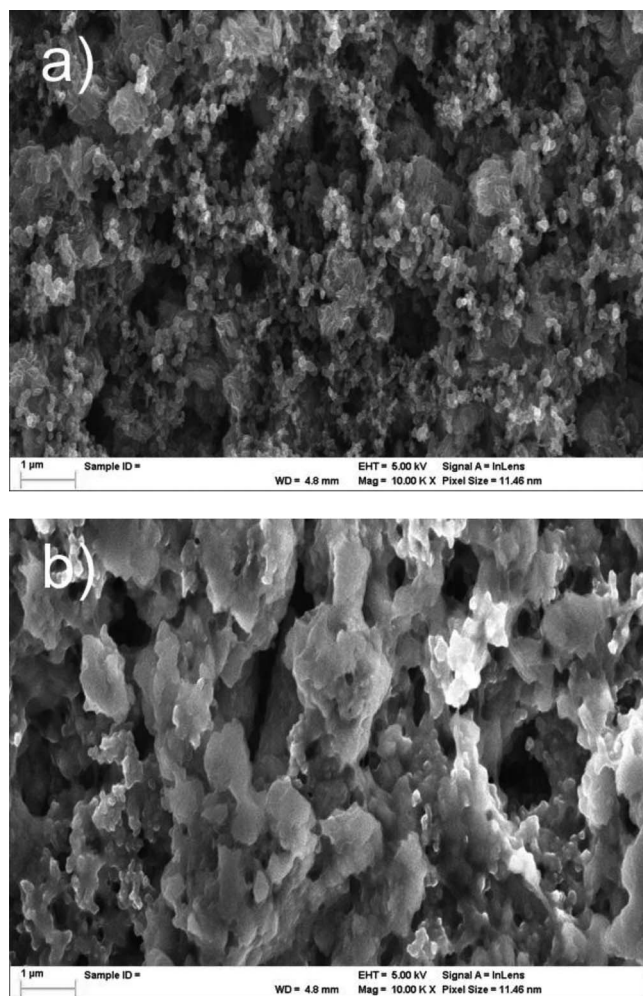

Figure 7. a) SEM image of a pristine TiO$_2$(B)-based electrode; b) ex situ performed SEM analysis of a cycled, desodiated electrode after 40 cycles.

of a pristine electrode (Figure 7a) with a cycled electrode (Figure 7b) clearly reveals the presence of a thick SEI layer.

Nevertheless, the structural reorganization and transformation of the starting material might additionally affect the impedance upon continuous (de-)sodiation. And, finally, it should be noted that also irreversible processes on the sodium metal surface have an impact on the overall resistance of the cell.

Conclusions

High surface area, nanocrystalline TiO$_2$(B) noodle-like secondary particles were successfully prepared by a facile one-pot synthesis, based on the hydrolysis of TiCl$_3$ using a mixture of ethylene glycol and water. In situ XRD and additional electrochemical studies reveal that the TiO$_2$(B) structure becomes fully amorphous within the first cycle. Besides, such electrodes, comprising environmentally friendly and non-toxic CMC as binder, show very interesting specific capacities at lower and elevated C rates of about 150, 120, 100, 90, 80, 70, and 50 mAh g^{-1} at 0.1, 0.2, 0.5, 1, 2, 5, and 10 C. However, a slight, but continuous decrease in capacity is observed upon cycling, presumably related to irreversible sodium trapping inside the host structure as well as the absence of a stable SEI, as evidenced by the continuously increasing internal resistance. Future studies addressing both aspects might involve the application of carbonaceous coatings to increase the electronic conductivity and enable the formation of a more stable SEI on the particles surface.

References

1. V. Palomares et al., *Energy Environ. Sci.*, **5**, 5884 (2012).
2. B. L. Ellis and L. F. Nazar, *Curr. Opin. Solid State Mater. Sci.*, **16**, 168 (2012).
3. H. Pan, Y.-S. Hu, and L. Chen, *Energy Environ. Sci.*, **6**, 2338 (2013).
4. M. D. Slater, D. Kim, E. Lee, and C. S. Johnson, *Adv. Funct. Mater.*, **23**, 947 (2013).
5. M. R. Palacin, Paper presented at the 17th International Meeting on Lithium Batteries (IMLB), June 10–14, 2014, Como, Italy.
6. M. Dahbi, N. Yabuuchi, K. Kubota, K. Tokiwa, and S. Komaba, *Phys. Chem. Chem. Phys.*, **16**, 15007 (2014).
7. V. L. Chevrier and G. Ceder, *J. Electrochem. Soc.*, **158**, A1011 (2011).
8. D. A. Stevens and J. R. Dahn, *J. Electrochem. Soc.*, **148**, A803 (2001).
9. R. Alcántara et al., *Carbon*, **41**, 3003 (2003).
10. R. Alcántara, P. Lavela, G. F. Ortiz, and J. L. Tirado, *Electrochem. Solid-State Lett.*, **8**, A222 (2005).
11. S. Komaba et al., *Adv. Funct. Mater.*, **21**, 3859 (2011).
12. S. Wenzel, T. Hara, J. Janek, and P. Adelhelm, *Energy Environ. Sci.*, **4**, 3342 (2011).
13. X. Xia and J. R. Dahn, *J. Electrochem. Soc.*, **159**, A515 (2012).
14. A. Ponrouch, A. R. Goñi, and M. R. Palacín, *Electrochem. Commun.*, **27**, 85 (2013).
15. L. Zhao et al., *Adv. Energy Mater.*, **2**, 962 (2012).
16. Y. Park et al., *Adv. Mater.*, **24**, 3562 (2012).
17. A. Abouimrane et al., *Energy Environ. Sci.*, **5**, 9632 (2012).
18. S. Wang et al., *Angew. Chem.*, **126**, 6002 (2014).
19. L. D. Ellis, T. D. Hatchard, and M. N. Obrovac, *J. Electrochem. Soc.*, **159**, A1801 (2012).
20. J. W. Wang, X. H. Liu, S. X. Mao, and J. Y. Huang, *Nano Lett.*, **12**, 5897 (2012).
21. S. Komaba et al., *Electrochem. Commun.*, **21**, 65 (2012).
22. S.-M. Oh et al., *Phys. Chem. Chem. Phys.*, **15**, 3827 (2013).
23. D.-J. Lee et al., *J. Mater. Chem. A* (2013).
24. Y. Xu, Y. Zhu, Y. Liu, and C. Wang, *Adv. Energy Mater.*, **3**, 128 (2013).
25. L. Baggetto et al., *J. Power Sources*, **234**, 48 (2013).
26. M. K. Datta et al., *J. Power Sources*, **225**, 316 (2013).
27. D. Bresser, F. Mueller, D. Buchholz, E. Paillard, and S. Passerini, *Electrochimica Acta*, **128**, 163 (2014).
28. J. Qian et al., *Chem. Commun.*, **48**, 7070 (2012).
29. L. Wu et al., *Energy Environ. Sci.*, **7**, 323 (2014).
30. L. Baggetto, J. K. Keum, J. F. Browning, and G. M. Veith, *Electrochem. Commun.*, **34**, 41 (2013).
31. R. Alcántara, M. Jaraba, P. Lavela, and J. L. Tirado, *Chem Mater*, **14**, 2847 (2002).
32. S. Hariharan, K. Saravanan, V. Ramar, and P. Balaya, *Phys. Chem. Chem. Phys.*, **15**, 2945 (2013).
33. F. Klein, B. Jache, A. Bhide, and P. Adelhelm, *Phys. Chem. Chem. Phys.*, **15**, 15876 (2013).
34. Z. Jian et al., *Chem. Commun.*, **50**, 1215 (2014).
35. P. Senguttuvan, G. Rousse, V. Seznec, J.-M. Tarascon, and M. R. Palacín, *Chem. Mater.*, **23**, 4109 (2011).
36. H. Pan et al., *Adv. Energy Mater.*, **3**, 1186 (2013).
37. A. Rudola, K. Saravanan, C. W. Mason, and P. Balaya, *J. Mater. Chem. A*, **1**, 2653 (2013).
38. Y. Sun et al., *Nat Commun*, **4**, 1870 (2013).
39. Y. Xu et al., *Chem. Commun.*, **49**, 8973 (2013).
40. L. Wu, D. Buchholz, D. Bresser, L. Gomes Chagas, and S. Passerini, *J. Power Sources*, **251**, 379 (2014).
41. K.-T. Kim et al., *Nano Lett.*, **14**, 416 (2014).
42. L. Wu et al., *Adv. Energy Mater.* (2014).
43. S.-M. Oh et al., *ACS Appl. Mater. Interfaces*, **6**, 11295 (2014).
44. H. A. Cha, H. M. Jeong, and J. K. Kang, *J. Mater. Chem. A*, **2**, 5182 (2014).
45. J. R. Gonzalez, R. Alcantara, F. Nacimiento, G. F. Ortiz, and J. L. Tirado, *CrystEngComm*, **16**, 4602 (2014).
46. H. Xiong, M. D. Slater, M. Balasubramanian, C. S. Johnson, and T. Rajh, *J. Phys. Chem. Lett.*, **2**, 2560 (2011).
47. J. P. Huang et al., *RSC Adv.*, **3**, 12593 (2013).
48. B. Zachau-Christiansen, K. West, T. Jacobsen, and S. Atlung, *Solid State Ion.*, **28–30**, 1176 (1988).
49. L. Kavan, M. Grätzel, S. E. Gilbert, C. Klemenz, and H. J. Scheel, *J. Am. Chem. Soc.*, **118**, 6716 (1996).
50. T. Ohzuku, T. Kodama, and T. Hirai, *J. Power Sources*, **14**, 153 (1985).
51. M. Wagemaker, W. J. H. Borghols, and F. M. Mulder, *J. Am. Chem. Soc.*, **129**, 4323 (2007).
52. D. Bresser et al., *J. Power Sources*, **206**, 301 (2012).
53. A. A. Belak, Y. Wang, and A. Van Der Ven, *Chem. Mater.*, **24**, 2894 (2012).
54. A. R. Armstrong, G. Armstrong, J. Canales, and P. G. Bruce, *Angew. Chem. Int. Ed.*, **43**, 2286 (2004).
55. A. R. Armstrong, G. Armstrong, J. Canales, R. García, and P. G. Bruce, *Adv. Mater.*, **17**, 862 (2005).
56. G. Armstrong, A. R. Armstrong, P. G. Bruce, P. Reale, and B. Scrosati, *Adv. Mater.*, **18**, 2597 (2006).
57. G. Armstrong, A. R. Armstrong, J. Canales, and P. G. Bruce, *Electrochem. Solid-State Lett.*, **9**, A139 (2006).
58. M. Zukalová, M. Kalbáč, L. Kavan, I. Exnar, and M. Graetzel, *Chem. Mater.*, **17**, 1248 (2005).
59. S. Brutti, V. Gentili, H. Menard, B. Scrosati, and P. G. Bruce, *Adv. Energy Mater.*, **2**, 322 (2012).
60. H. Liu et al., *Adv. Mater.*, **23**, 3450 (2011).
61. G. Xiang, T. Li, J. Zhuang, and X. Wang, *Chem. Commun.*, **46**, 6801 (2010).
62. D. Bresser et al., *Adv. Energy Mater.*, **3**, 513 (2013).
63. D. Bresser et al., *Chem. Mater.*, **25**, 4977 (2013).
64. Z. Bi et al., *J. Power Sources*, **222**, 461 (2013).
65. K. T. Lee et al., *Energy Environ. Sci.* (2013).
66. K. Brezesinski et al., *J. Am. Chem. Soc.*, **132**, 6982 (2010).
67. V. Augustyn et al., *Nat Mater*, **12**, 518 (2013).
68. J. Song, H. Lee, Y. Wang, and C. Wan, *J. Power Sources*, **111**, 255 (2002).
69. C. Wang, A. J. Appleby, and F. E. Little, *Electrochimica Acta*, **46**, 1793 (2001).